A Shape-Based Inversion Algorithm Applied to Microwave Imaging of Breast Tumors

Reza Firoozabadi, Eric L. Miller, *Senior Member, IEEE*

Abstract—We propose a new shape-based inversion algorithm to identify an anomaly embedded in an inhomogeneous layered geometry. More specifically, we apply our approach to microwave breast imaging where the geometry consists of several inhomogeneous layers and the potential tumor is embedded in the innermost layer. In addition to the tumor identification, we estimate the irregular transition layer between the breast inner layers by a sharp boundary. We also perform the sensitivity study by perturbation of the dielectric properties of the breast layers from their mean values in the inverse problem. Our inversion algorithm utilizes a low-dimensional parametric form of the geometry, and a low-dimensional model for presentation of the dispersive dielectric properties. The algorithm uses multiple-frequency multi-source data and the weak scattered fields contribute to the estimation of the unknowns. Several numerical examples are provided to evaluate the effectiveness of our approach. The results prove the accuracy and robustness of our approach despite the complex geometry and the simplified inverse model.

Index Terms—microwave imaging, antenna arrays, parametric modeling, dispersive media, inverse problems, nonlinear estimation, spline functions

I. INTRODUCTION

Based on the latest American Cancer Society report [1], breast cancer is the second most common cancer and the second cause of cancer deaths in US women. Early detection of breast tumors will critically reduce the mortality rate in women. Currently, standard screen film mammography [2], MRI [3], [4] and ultrasound [5] are the imaging modalities used for early breast cancer detection. Microwave tomography is a complementary imaging technique which uses the contrast between the tissues. High contrast between normal breast tissue and the malignant tissue, as well as its accessibility and transparency to microwaves, makes this modality a good option for breast cancer detection. Low power non-ionizing radiation and suppression of breast compression are the other advantages of this method [6]. A novel tomography modality is current-injection electrical impedance tomography (EIT) where the shape-based inversion solutions are utilized [7].

In microwave imaging, an array of antennas sequentially illuminate the breast in a multistatic approach. The consequent scattered fields are recorded by the receiving antennas and used to identify the tumor by reconstructing its boundary or creating the spatial profile of dielectric properties in the region of interest containing the tumor.

There are two categories of imaging techniques in literature. In the first category, called inverse scattering methods, a complete or partial map of dielectric properties in the desired region is reconstructed from the measured scattered fields by fitting the data to the predicted scattered fields. A clinical group in Dartmouth College [8]–[10] has been working on this category of breast imaging algorithms. Their imaging system consists of a tank filled with a coupling medium, with the breast immersed in it through a hole. The circular array of transmitter/receiver antennas surrounding the breast illuminates it and collects the scattered fields to be utilized in the reconstruction algorithm. Another research group in University of Wisconsin is also performing comprehensive research on 3-D microwave breast cancer detection [11]–[13]. A group in Duke University [14]–[16] and another one in Carolinas Medical Center [17], [18], have also been working on this category of imaging methods.

In the second category of imaging techniques known as radar methods, the location of the strongly scattering anomaly is estimated directly, rather than recovering a detailed map of the pixels. The first system of this category for breast cancer detection was developed by Hagness and colleagues [19]–[21]. Radar-based approaches use ultra-wideband signals with a bandwidth of several gigahertz. A number of locations surrounding the breast are scanned by an antenna. The same antenna collects the back-scattered waves and this process is repeated. The reflections at different locations are then focused by computing the travel time between the sensor and the focal point and application of a time-shifting and summing method. This method is based on the idea that reflections from the tumor add coherently, but the reflection from clutters add incoherently. This category of methods takes advantage of the simpler imaging algorithms and is thus less computationally complex.

Our iterative approach uses an inversion technique similar to the first category of imaging methods where the optimization is done in the frequency domain. However, since our primary objective is describing the geometry of the tumor (should one exist) and the intervening tissue layers, we focus on direct estimation of the unknown boundaries, instead of complete estimation of the dielectric profile. In this respect, our method is similar to the second category of imaging methods in that we localize the tumor and additionally characterize its spatial structure. We estimate the boundary of the anomaly inserted in a breast cross-section consisting of several inhomogeneous layers as well as the smooth transition layer between the inner layers. The entire geometry is surrounded by an array of transmitting/receiving microwave antennas which operate in multiple-frequency multi-source mode: Each antenna radiates at any single frequency, while the other non-adjacent antennas collect the electromagnetic field data. Our iterative inversion algorithm optimizes the unknowns, parameterized in low-dimensional form, by fitting the measured field data to the ones predicted by a forward model at each step until the

convergence is met.

Our approach is particularly adapted to processing coronal cross sections of the breast. A coronal slice of the breast consists of multiple layers where the tumor is typically located in the innermost layer. The breast with denser geometry is more adapted to our approach as we can distinguish the layers more accurately. The numerical results prove that our approach performs very well in presence of all the inverse model discrepancies with the actual geometry. These mismatches include the breast layered inhomogeneity estimated by homogenous layers, transition layer between inner layers estimated by a sharp boundary, the arbitrary irregular tumor boundary estimated by a circle, and the possible perturbation of mean dielectric properties from their actual values.

The paper is organized as follows. In Section II we describe the problem and the physical solution in detail. In Section III, we present the formulation to parameterize the boundaries in low-dimensional form. In Section IV, we present the parameterization of the dielectric properties in a microwave range of frequencies. Inversion algorithm is introduced and described in Section V. Numerical examples are presented and the results are discussed in Section VI. Concluding remarks are given in Section VII.

II. PROBLEM STATEMENT

In this paper we study our inversion approach applied to breast tumor detection problem where the geometry consists of breast coronal slices. Each slice is composed of several inhomogeneous layers including skin, adipose (fat), and fibroglandular. The breast anatomy is characterized by a smoothly varying transition between the inner layers (adipose and fibroglandular). The tumor is assumed to have an arbitrary irregular shape and to be located in the fibroglandular layer. A simplified 3-D geometry of breast is illustrated in Figure 1. The Figure 2 displays a sample coronal slice. As shown in Figure 2, the breast is taken to be submerged in a coupling liquid. A circular array of transmitter/receiver antennas embraces the breast. Each antenna operates in either transmit or receive mode. At any moment, one antenna operates as transmitter and the other non-adjacent ones acquire the field data.

Electromagnetic field components satisfy Maxwell's equations and radiation condition in each breast layer which is characterized by its inhomogeneous complex dielectric properties. With the antennas located in z direction, a TE wave is propagated in the $x - y$ plane and the Helmholtz equation in source-free space is [22]

$$(\nabla^2 + k^2(x,y))E_z(x,y) = 0 \qquad (1)$$

and

$$k(x,y) = \omega \sqrt{\varepsilon_0 \mu_0 \left(\varepsilon_r(x,y) + i\frac{\sigma(x,y)}{\omega \varepsilon_0} \right)} \qquad (2)$$

where ∇^2 is the 2-D Laplacian operator, k is the wave number, E_z is the electric field in z direction, ω is the angular frequency, ε_0 is the free space permittivity, μ_0 is the free space permeability, ε_r is the relative permittivity of medium, and σ is the medium conductivity. We make use of FDFD forward model to discretize the Helmholtz equation and simulate the
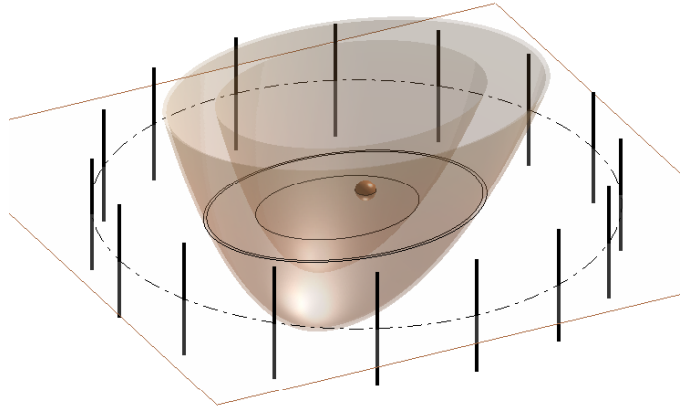

Fig. 1. Simplified 3D geometry: Breast layers with the tumor located in the most inner layer. A circular array of uniformly distributed antennas encloses the entire breast.
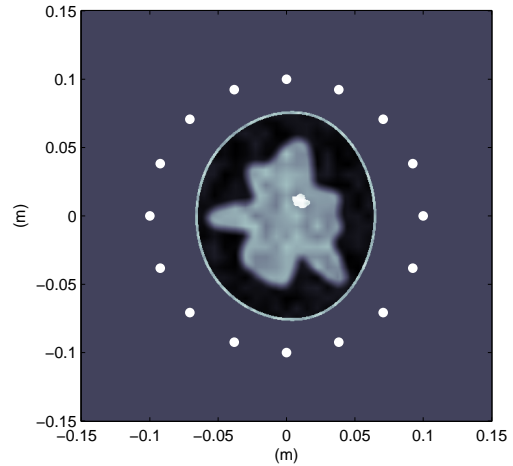

Fig. 2. The geometry of a breast slice consists of skin layer, adipose layer, and fibroglandular layer from the outer to the inner. The tumor is embedded in the fibroglandular layer. The entire breast is immersed in the coupling liquid and surrounded by antennas.

propagation of electromagnetic waves in breast layers [23]. In order to solve the open-region problem, we use an eight-grid cell Perfect Matched Layer (PML) absorbing boundary condition [24].

Our ultimate objective is to identify the tumor location and its size in a breast slice from the observed field data collected by the antenna array. The fields scattered by breast are functions of the geometry and dispersive dielectric properties of the breast tissues. In our approach, we attempt to find the unknown parameters by reducing the misfit between the observed field data and the field data predicted by the forward model in an iterative procedure. Specifically, our inverse algorithm minimizes a cost function based on the least-squares formulation as follows

$$c(\mathbf{u}) = \frac{1}{2}\|\mathbf{f}(\mathbf{u}) - \mathbf{f_0}\|_2^2 \qquad (3)$$

where $\mathbf{f}(\mathbf{u})$ is the field vector calculated by forward solver at the receivers for the predicted geometry characterized by the unknown vector $\mathbf{u}$, and $\mathbf{f}_0$ is the noisy observed field vector. Mathematically we seek a vector $\hat{\mathbf{u}}$ to satisfy the following equation

$$\hat{\mathbf{u}} = \arg \min_{\mathbf{u}} c(\mathbf{u}) \qquad (4)$$

III. PARAMETERIZATION OF GEOMETRY

Many shape parameterization options are available in literature such as Fourier descriptors [25], Lagrange Interpolation [26] and parametrically defined shapes [27], [28] based on global representation of the geometry, as well as B-splines [29]–[31] where the control points determine the properties of the curve. We choose B-splines to model the irregular transition layer between adipose and fibroglandular layers where the control points determine the shape of boundary. While we could model the tumor as well using a B-spline approach, we have found that for small tumors, one cannot stably recover fine scale geometric structures especially in the face of uncertainty in the geometry and electromagnetic contrasts of the adipose and fibroglandular layers. Hence in this paper, we characterize the tumor as a circular object and recover the two coordinates of the center as well as the radius. The geometric parameters that we estimate are then comprised of the interface control point coordinates, and the three parameters describing the tumor.

B-splines are piecewise polynomial functions providing local approximation to curves using a small number of parameters called control points. A curve is defined in B-spline parametric form with basic functions associated with m control points $\mathbf{p}_i$ as [30]

$$\mathbf{P}(t) = \sum_{i=1}^{m} \mathbf{p}_i N_{i,k}(t) \quad \text{for} \quad t_k \leq t < t_{m+1} \qquad (5)$$

with the basis functions $N_{i,k}(t)$ defined by the recurrence relations

$$N_{i,1}(t) = \begin{cases} 1, & \text{if } t_i \leq t < t_{i+1} \\ 0, & \text{otherwise} \end{cases} \qquad (6a)$$

$$N_{i,k}(t) = \frac{t - t_i}{t_{i+k-1} - t_i} N_{i,k-1}(t) + \frac{t_{i+k} - t}{t_{i+k} - t_{i+1}} N_{i+1,k-1}(t) \qquad (6b)$$

where $T = \{t_1, t_2, ..., t_{m+k}\}$ is called the knot vector with $t_1 < t_2 < ... < t_{m+k}$.

There is a linear relationship between the coordinates of curve points and their associated control points. To change the curve shape, the control point locations are adjusted while the other parameters are fixed. The ends of a curve can be joined to make a closed loop. In order to keep the C^{k-2} continuity of the closed curve, the first $k-1$ control points must repeat at the end. Figure 3 shows the steps to create a closed boundary by B-spline functions.

The interface between inner layers is modeled by closed cubic B-Splines where the 2-D control points are defined by $\mathbf{p}_i = [p_{x,i}, p_{y,i}]^T$, $i = 1, 2, ..., N_{u,int} + 3$ with $\mathbf{p}_j = \mathbf{p}_{j+N_{u,int}}, j = 1, 2, 3$ where $N_{u,int}$ is the number of interface boundary control points. For our approach the control point positions are converted to polar coordinates where the coordinates center is the determined by the average of control
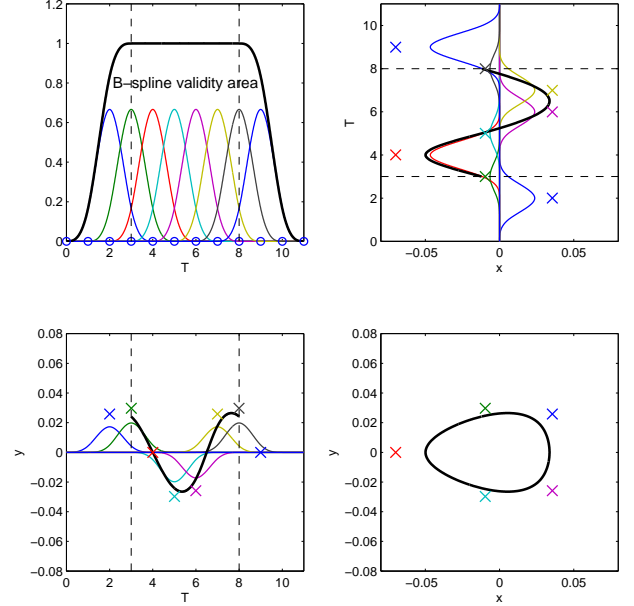

Fig. 3. (Upper-left) basis functions (thin lines) and their summation (bold line) vs. knots, (Upper-right) basis functions weighted by x component of control points (thin lines) and x-variation of final curve vs. knots (bold line), (Lower-left) basis functions weighted by y component of control points (thin lines) and y-variation of final vs. knots (bold line), (Lower-right) final closed curve. In all figures, knots are indicated by 'o' and control points by '×'.

points coordinates. Control points are separated by equal angles and are identified only by the radius R_l, $l = 1, ..., N_{u,int}$. The interface is then parameterized by unknown sub-vector

$$\mathbf{u}_{int} = \begin{bmatrix} R_1, R_2, ..., R_{N_{u,int}} \end{bmatrix}^T \qquad (7)$$

The tumor is modeled by the unknown center coordinates and its radius, parameterized by the unknown sub-vector

$$\mathbf{u}_{tum} = [C_x, C_y, R_{tum}]^T \qquad (8)$$

The geometry unknown vector is then defined as

$$\mathbf{u} = \begin{bmatrix} \mathbf{u}_{tum}{}^T, \mathbf{u}_{int}{}^T \end{bmatrix}^T \qquad (9)$$

In order to discretize the problem geometry for implementation of FDFD forward model in a manner which respects the B-spline representation of the object boundaries, we make use of a filling algorithm which searches in the pixels and marks the ones inside the region enclosed by each boundary, including the border itself, starting from the outermost boundary. This approach is basically a staircase approximation to the B-spline boundary. By using a very small grid-size, the desired discretization accuracy is achieved.

IV. PARAMETERIZATION OF DIELECTRIC PROPERTIES

In microwave breast imaging, knowing the dielectric properties of breast tissues and malignant tumors over the desired frequency range is necessary. A series of publications have documented the dielectric properties of biological tissues, including breast tissues, extracted from measurements over

various frequency ranges [32]- [42]. Most of the reported studies suggest that there is a large contrast between the normal and malignant breast tissues. Water content level plays the major role in the value of dielectric properties of tissue. Low water content tissues (such as fat) have lower conductivity and permittivity values, while the ones with high water content (such as skin and muscle) show higher dielectric properties.

A number of approaches have been proposed in the literature to model the frequency-dependent dielectric properties of dispersive media from the measured data, including recursive convolution [43], auxiliary differential [44], and z-transform [45]. These approaches are different in implementation, accuracy and the computational cost. Debye formulation of the first or second order has been widely used to model the dispersive media [44]. This model fits the equation coefficients to the measured data and determines the relation between the electric displacement and electric field. First-order Debye model is of the form

$$\varepsilon_{rc}(\omega) = \varepsilon_r(\omega) + i\frac{\sigma(\omega)}{\omega\varepsilon_0} = \varepsilon_\infty + \frac{\varepsilon_s - \varepsilon_\infty}{1 - i\omega\tau} + i\frac{\sigma_s}{\omega\varepsilon_0} \quad (10)$$

where ε_{rc} is the relative complex permittivity, ω is the angular frequency, ε_r is the relative permittivity, σ is the conductivity, ε_0 is the free space permittivity, ε_∞ is the relative permittivity at infinite frequency, ε_s is the static relative permittivity, τ is the relaxation time constant, and σ_s is the static conductivity.

We use the first-order Debye model in our work as despite its simplicity, it models the dielectric properties very well in one frequency decade. Figures 4(a) and 4(b) illustrate the typical values for dielectric properties of breast tissues versus frequency in skin, adipose, fibroglandular and tumor using first-order Debye model [39], [46].

V. INVERSION ALGORITHM

Our inverse problem is posed in a variational context requiring the solution to a nonlinear least squares optimization problem. A variety of methods are present in the literature to solve such problems including descent type methods. In this category of solutions, by knowing the object function in analytical form, the solution is achieved iteratively using the gradient information. Steepest decent, Gauss-Newton, conjugate gradient, and Levenberg-Marquardt methods are in this category. Among all these methods, we choose Levenberg-Marquardt [47], [48] which is basically a trade-off between steepest descent approach which is slow to converge and Gauss-Newton method which can be unstable if the Jacobian matrix is poorly conditioned. The conditioning is dealt with in an adaptive manner through the choice of a conditioning parameter at each iteration. In many cases, this algorithm is more efficient than some other numerical methods such as steepest descent and conjugate gradient [49].
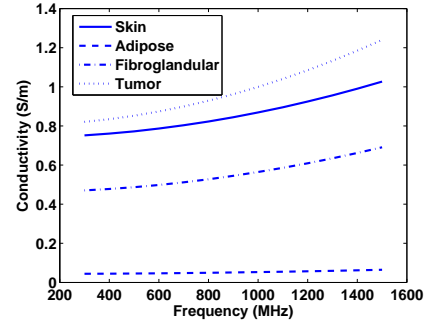
Our inversion method minimizes the cost function

$$c(\mathbf{u}) = \frac{1}{2}\|\mathbf{r}(\mathbf{u})\|_2^2 = \frac{1}{2}\mathbf{r}^H(\mathbf{u})\mathbf{r}(\mathbf{u}) \quad (11)$$

where $\mathbf{r}(\mathbf{u}) = \mathbf{f}(\mathbf{u}) - \mathbf{f_0}$ is the residual vector, $\mathbf{f}(\mathbf{u})$ is the field vector calculated by forward solver at the receiver locations for the predicted geometry, $\mathbf{u}$ is the unknown vector, $\mathbf{f}_0$ is the
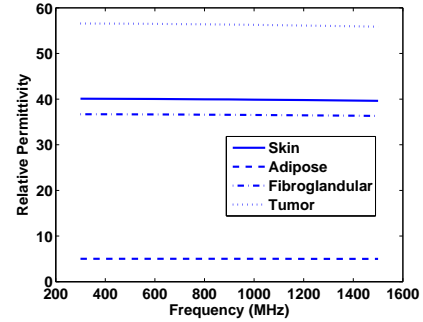
(a) Relative permittivity

(b) Conductivity

Fig. 4. Typical values for dielectric properties of breast tissues (skin, adipose, fibroglandular) and tumor. (a) Relative permittivity. (b) Conductivity.

noisy observed field data vector and $\mathbf{r}^H(\mathbf{u})$ is the transposed complex conjugate vector of $\mathbf{r}(\mathbf{u})$.

Levenberg-Marquardt iterative algorithm uses the following update formula to calculate the unknown vector in $(n+1)$th step, starting from an initial guess $\mathbf{u}^{(0)}$ [50]

$$\mathbf{u}^{(n+1)} = \mathbf{u}^{(n)} - \mathbf{d}^{(n)} \quad (12)$$

$$\mathbf{d}^{(n)} = \left(\nabla^2 c(\mathbf{u}^{(n)}) + \lambda^{(n)}\mathbf{I}_{N_u}\right)^{-1}\nabla c(\mathbf{u}^{(n)}) \quad (13)$$

where ∇c and $\nabla^2 c$ are gradient vector and Hessian matrix of the cost function defined in Equation (11), respectively, N_u is the number of unknowns, $\mathbf{I}_{N_u}$ is the identity matrix of dimension N_u, and λ is the Levenberg-Marquardt parameter being updated in each iteration. Complex-valued matrix calculations lead to

$$\nabla c(\mathbf{u}^{(n)}) = \text{Re}\left(\mathbf{J}^H(\mathbf{u}^{(n)})\mathbf{r}(\mathbf{u^{(n)}})\right) \quad (14)$$

$$\nabla^2 c(\mathbf{u}^{(n)}) \approx \text{Re}\left(\mathbf{J}^H(\mathbf{u}^{(n)})\mathbf{J}(\mathbf{u^{(n)}})\right) \quad (15)$$

or

$$\mathbf{d}^{(n)} \approx \left(\text{Re}\left(\mathbf{J}^H(\mathbf{u}^{(n)})\mathbf{J}(\mathbf{u^{(n)}})\right) + \lambda^{(n)}\mathbf{I}_{N_u}\right)^{-1}$$
$$\text{Re}\left(\mathbf{J}^H(\mathbf{u}^{(n)})\mathbf{r}(\mathbf{u^{(n)}})\right) \quad (16)$$

To solve the above equation, we need to calculate the Jacobian matrix. In the Appendix, we summarize the procedure to calculate the Jacobian matrix in a multiple-frequency multi-source problem.

A block diagram of our inversion algorithm is illustrated in Figure 5. The algorithm starts with an initial guess of
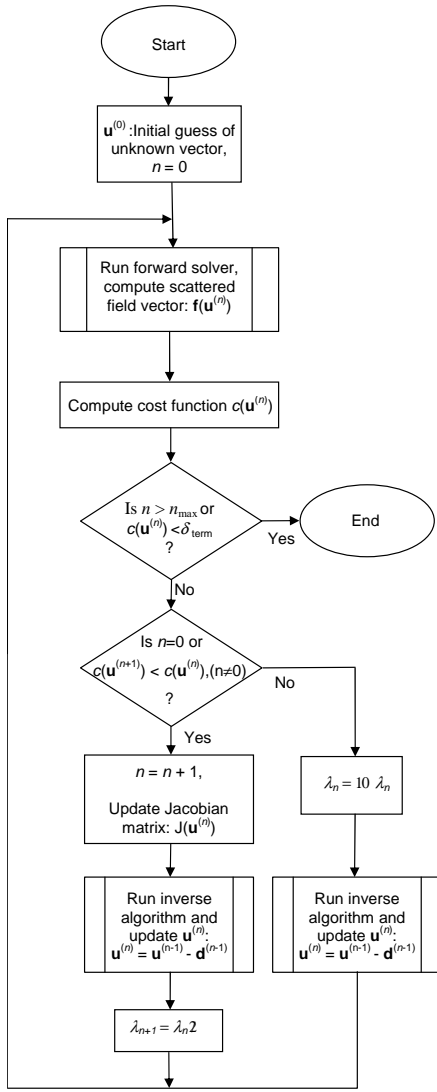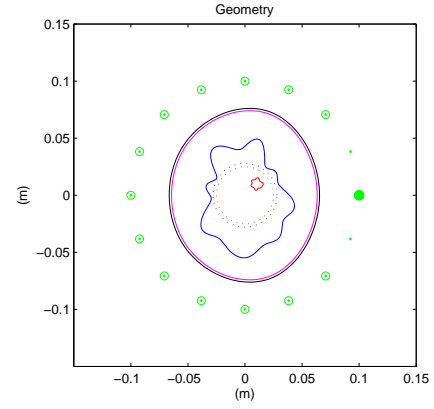
Fig. 5. The inversion algorithm block diagram

Fig. 6. Example1: Breast coronal cross-section geometry includes the tumor with average diameter of 1 cm, the interface between adipose and fibroglandular layers and the skin layers. Tumor initial guess (inner dotted line) and interface initial guess (outer dotted line) are also shown. In this figure, one antenna is in transmitting mode (bold antenna) and the other non-adjacent antennas in receiving mode (encircled antennas).

VI. NUMERICAL RESULTS

In this section, we present several numerical examples to support the concept of our inversion algorithm. We study the identification of tumors of different sizes, the behavior when there is no tumor, reconstruction with low contrast between tumor and fibroglandular layer, and sensitivity to perturbation of dielectric properties from their mean values.

Breast coronal cross-section, consisting skin layer, adipose layer, fibroglandular layer and the tumor, immersed in a coupling liquid, was illustrated in Figure 2. Typical average values for relative permittivity and conductivity of the breast tissue versus frequency were also plotted in Figures 4(a) and 4(b), respectively. In all following examples, for the actual geometry, inhomogeneity in dielectric properties of the layers is modeled by a standard normal distribution around the average values in Figure 4. A standard deviation of 10% is applied to the relative permittivity and conductivity of skin, adipose and fibroglandular layers, and 5% is applied to the tumor. There is a smooth transition layer between adipose and fibroglandular layers which is modeled by a Gaussian blur filter. Matching liquid is assumed to be a 60% glycerine solution with $\epsilon_r = 47$ and $\sigma = 1.36$ S/m in all frequencies. The breast external surface is assumed to be known and the skin layer width is taken to be 2 mm. The unknown boundaries to reconstruct are the transition layer between fibroglandular and adipose layers estimates by a closed B-spline curve using a limited number of control points, and tumor modeled by a circle with an unknown center and radius. A circular array of 16 multiple-frequency transmitter/receiver antennas illuminates the breast by one antenna radiating at a single-frequency at a time while the other 13 non-adjacent antennas collect the fields. In our examples, we use only four transmitting antennas 90 degrees apart. Noisy data are simulated by adding Gaussian noise to the real and imaginary parts of the noise-free data generated by the forward solver using a finer finite difference grid. Simulations are performed in multiple-frequency mode at 600, 900, and 1200 MHz. Signal to noise ratio is assumed to be 40

unknown parameters vector $\mathbf{u}^{(0)}$. The forward solver is run with the initial parameters and computes the initial predicted field vector $\mathbf{f}(\mathbf{u}^{(n=0)})$. The initial cost function $c(\mathbf{u}^{(n=0)})$ is computed using the predicted field vector and the observed data from the actual geometry $\mathbf{f_0}$ using Equation (11). In the next step ($n = 1$), the Jacobian matrix for the predicted unknown parameters $\mathbf{J}(\mathbf{u}^{(n=1)})$ is calculated as explained in the Appendix. The inversion algorithm is then run using Equations (14)-(16) starting with a small initial λ and updates the unknown vector using Equation (12). We decrease λ by half and repeat the algorithm using the updated unknown vector and updated λ. If the cost function increases in the next step, we increase λ by a factor of ten, run the inverse algorithm and find the updated unknown vector using this larger parameter, and continue the algorithm. The algorithm is terminated if the cost function becomes less than a pre-defined threshold (δ_{term}) or the maximum number of iterations ($n_{\max}$) is reached.
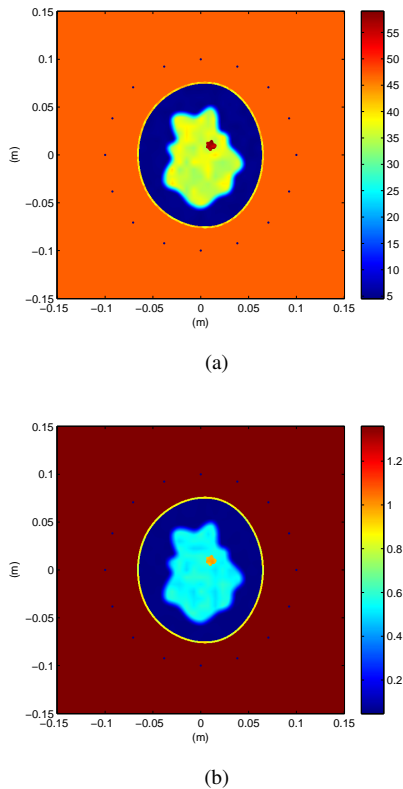
(a)

(b)

Fig. 7.   Example 1: Spatial distribution of dielectric properties at 900 MHz. (a) Relative permittivity distribution. (b) Conductivity distribution (S/m).
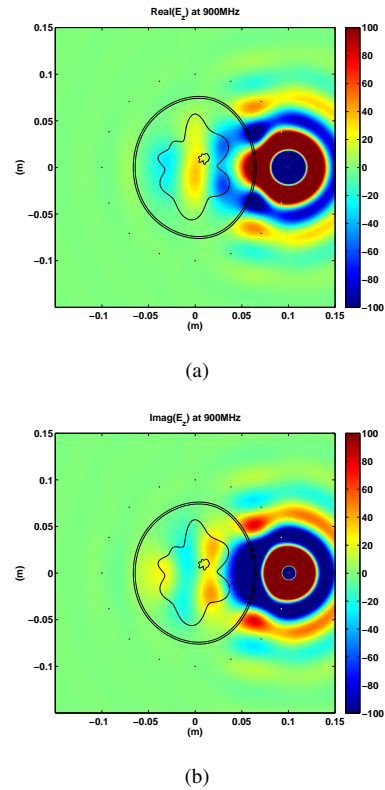

(a)

(b)

Fig. 8.   Example 1: Electric field plot at 900 MHz. The magnitude is truncated in order to provide a better illustration of the fields. (a) Real Part. (b) Imaginary part.

dB in all examples.

In Examples 1-3, the data are generated using the actual geometry mentioned above. In our inverse problem, we use the frequency-dependent average dielectric properties of the tissues extracted from the typical values shown in Figures 4(a) and 4(b). In these examples, 15 control points are used to reconstruct the interface between adipose and fibroglandular layers. With 3 tumor unknowns and 15 interface unknowns, the total number of unknowns is 18. Also with 3 operating frequencies and 4 different transmitting antennas, there are 12 sets of data.

In Example 1, the tumor with average diameter of 10 mm is reconstructed along with the interface between adipose and fibroglandular layers in just a few iterations. Figure 6 shows the ground truth geometry. The spatial distributions of relative permittivity and conductivity at 900 MHz are plotted in Figure 7 for the entire cross-section. Figure 8 displays the real and imaginary parts of the electric fields at 900 MHz where one antenna is radiating as shown in Figure 6. The magnitude of the electric field is truncated in order to provide a better illustration of the fields. The reconstructed geometry and the cost function vs. the iterations are shown in Figure 9. The results state that starting from a far initial guess for boundaries (shown in Figure 6), the convergence to actual boundaries is achieved only in 7 steps.

A smaller tumor is studied in Example 2 where the average diameter is 5 mm. Figure 10(a) shows the ground truth geometry and the initial guesses for both boundaries. The

reconstructed geometry is shown in Figure 10(b). As shown in this figure, still we can estimate the interface boundary and localize the tumor with proper accuracy.

We study the case with no tumor in Example 3. The inverse problem is started from the initial boundaries shown in Figure 11(a). By performing our inversion algorithm, we observe that the predicted tumor vanishes by converging into a point while the other interface is still reconstructed well. Figure 11(a) shows the geometry including the initial guesses for both boundaries. The reconstructed geometry is displayed in Figure 11(b).

In example 4, we study the capability of algorithm in reconstruction of the geometry with low contrast between the tumor and the fibroglandular layer. We use the same geometry in Example 1, but reduce the frequency-dependent average dielectric properties of the tumor very close to those of the fibroglandular layer, as shown in Figures 12(a) and 12(b). The reconstructed geometry is illustrated in Figure 13. As shown in the figure, even with very low contrast, we can estimate the interface boundary very well and localize the tumor with a good accuracy.

In the remaining two examples we examine the sensitivity of our approach to perturbation of the dielectric properties. The observed field data are again simulated using the inhomogeneous geometry mentioned before. But the inverse algorithm uses perturbed complex permittivity values by deviating the typical average vales in Figures 4(a) and 4(b). We use a very rough interface between the breast inner layers in these
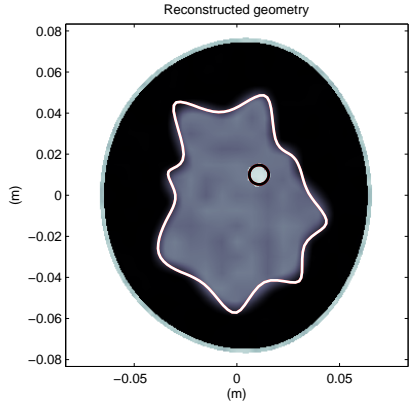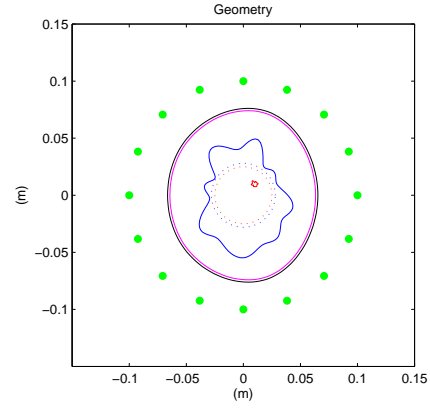
(a)
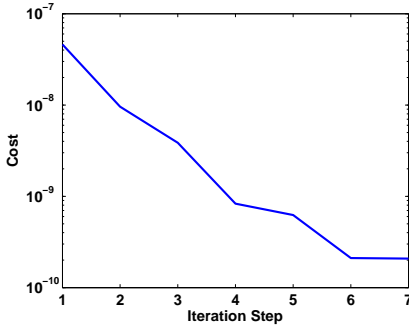
(b)

Fig. 9. Example 1: Inversion results. (a) Reconstructed boundaries for tumor and the interface (solid lines) vs. true geometry starting from the initial boundaries shown in Figure 6. (b) Cost function vs. iteration steps.
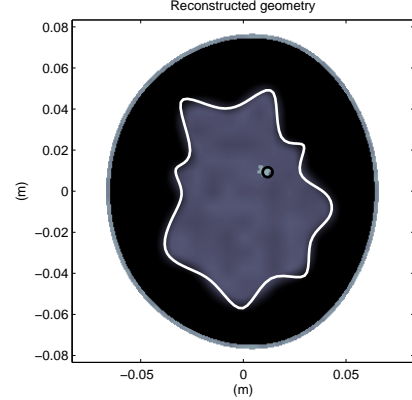

(a)

(b)

Fig. 10. Example 2: (a) Breast coronal cross-section geometry and the initial guess, where the tumor has average diameter of 5 mm. (b) Reconstructed boundaries for tumor and interface (solid lines) vs. true geometry starting from the initial boundaries shown in Figure 10(a).

examples. By using a limited number of control points, we still get a good estimate of the interface, and the tumor is identified well. We make use of 20 control points to estimate the interface between the breast inner layers. With 3 unknowns for the tumor and 20 for the interface, the total number of unknowns is 23. Also with 3 operating frequencies and 4 different transmitting antennas, there are 12 sets of data.

In Example 5, the typical complex permittivity average values of skin and tumor are perturbed by 15% increase for use in the inversion algorithm. Adipose and fibroglandular layers are also perturbed by 15% decrease in their complex permittivity from the typical average values. The actual geometry and the initial guesses for both boundaries are shown in Figure 14(a). Reconstructed geometry is illustrated in Figure 14(b) where it is observed that good convergence is achieved by our inversion algorithm in 9 steps for both the interface between inner layers and the tumor. The cost function versus the iteration steps is also plotted in Figure 14(c).

In Example 6, the typical average values of dielectric properties of the breast layers and the tumor are perturbed by 10% for use in the inversion algorithm where the perturbation is positive for skin and tumor layers and negative for adipose and fibroglandular layers. The geometry and initial guesses for both boundaries are shown in Figure 15(a). Figure 15(b) displays the good convergence achieved in 11 steps by our inversion algorithm for both the tumor and the interface

between the inner. The cost function versus the iteration steps is also plotted in Figure 15(c).

VII. CONCLUSION

A new shape-based inversion algorithm was proposed for detection of anomaly in a multi-layer sliced geometry and was applied to the problem of breast cancer detection successfully. In our approach, breast geometry and dielectric properties are modeled in low-dimensional parametric form. We provided examples to prove that despite the complex geometry and imperfections in the inverse model, our algorithm is robust and can identify the tumor and the unknown interface very well. Geometry variations were studied including the tumors of different sizes, the breast slice lacking the tumor, and perturbation of dielectric properties in inversion algorithm from their actual mean values.

The results suggest that the tumor is identified pretty well in all studied examples. Our method is more adapted to denser breasts as the inner layers can be distinguished more accurately. The future work includes the extension to 3-D reconstruction of anomaly, use of clinical data as the input to our approach, fusion with MRI-extracted geometry, and
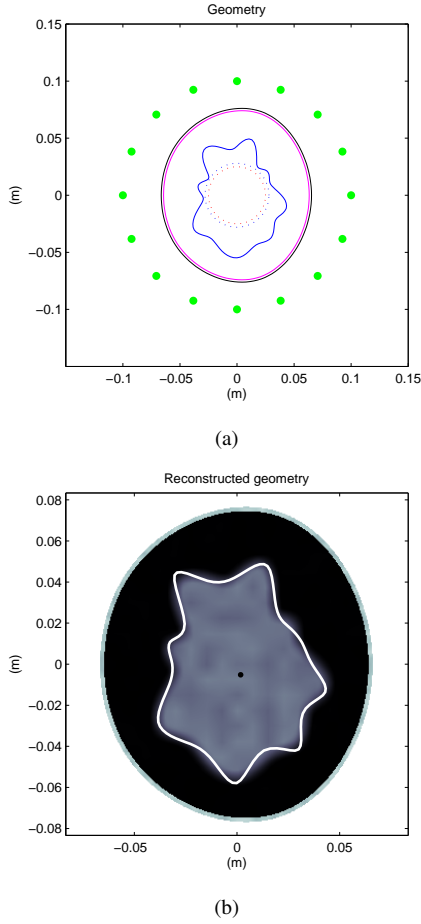
(a)

(b)

Fig. 11.   Example 3: (a) Breast coronal cross-section geometry in absence of tumor. (b) Reconstructed boundaries for tumor and interface (solid lines) vs. true geometry starting from the initial boundaries shown in Figure 11(a).

simultaneous estimation of the geometry and the dielectric properties of the breast tissues.

Although the numerical results prove that the convergence met in our problem provides accurate reconstruction, even with far initial guesses inside the geometry, we may consider global or hybrid optimization approaches in which a global method is used to get a good initial guess for local method. This is left as a future work.

APPENDIX

A. Derivation of Jacobian Matrix and Residue Vector

In a multi-frequency multi-source problem with N_f operating frequencies and N_{rec} receiving antennas, the residue subvector and the Jacobian sub-matrices at frequency f_i and for the radiating antenna a_i are as follows

$$\mathbf{r}(f_i, a_i, \mathbf{u}) = \mathbf{f}(f_i, a_i, \mathbf{u}) - \mathbf{f}_0(f_i, a_i) \qquad \text{(A-1)}$$

$$\mathbf{J}_{tum}(f_i, a_i, \mathbf{u}) = \frac{\partial \mathbf{r}(f_i, a_i, \mathbf{u})}{\partial \mathbf{u}_{tum}} = \begin{bmatrix} \frac{dr_1}{dc_x} & \frac{dr_1}{dc_y} & \frac{dr_1}{dr_{tum}} \\ \frac{dr_2}{dc_x} & \frac{dr_2}{dc_y} & \frac{dr_2}{dr_{tum}} \\ \vdots & \vdots & \vdots \\ \frac{dr_{N_r}}{dc_x} & \frac{dr_{N_r}}{dc_y} & \frac{dr_{N_r}}{dr_{tum}} \end{bmatrix}$$
(A-2)

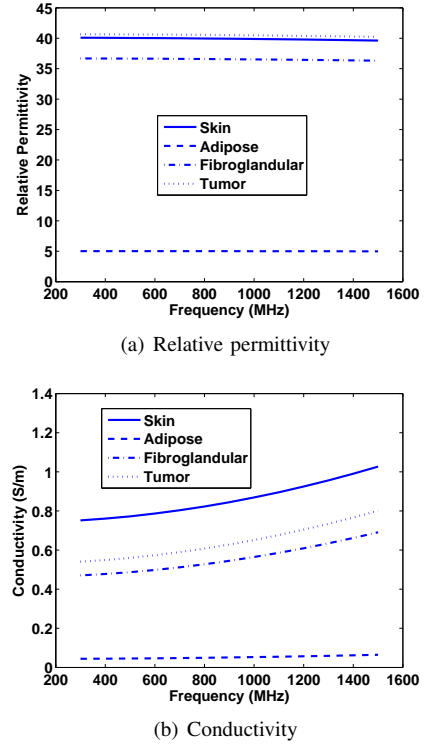(a) Relative permittivity

(b) Conductivity

Fig. 12.   Dielectric properties of breast tissues (skin, adipose, fibroglandular) and tumor, with low contrast between tumor and the fibroglandular layer, used in Example 4. (a) Relative permittivity. (b) Conductivity.
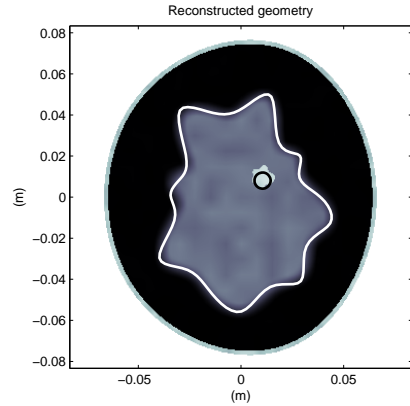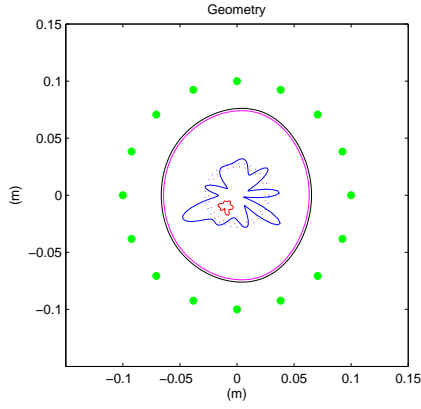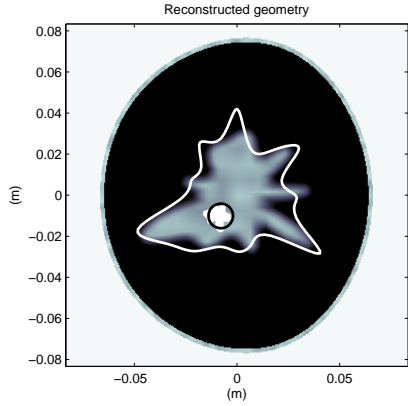

Fig. 13.   Example4: Reconstructed boundaries for tumor and interface (solid lines) vs. true geometry starting from the initial boundaries in Figure 6.

$$\mathbf{J}_{int}(f_i, a_i, \mathbf{u}) = \frac{\partial \mathbf{r}(f_i, a_i, \mathbf{u})}{\partial \mathbf{u}_{int}} = \begin{bmatrix} \frac{dr_1}{dR_1} & \frac{dr_1}{dR_2} & \cdots & \frac{dr_1}{dR_{Nu}} \\ \frac{dr_2}{dR_1} & \frac{dr_2}{dR_2} & \cdots & \frac{dr_2}{dR_{Nu}} \\ \vdots & \vdots & \ddots & \vdots \\ \frac{dr_{N_r}}{dR_1} & \frac{dr_{N_r}}{dR_2} & \cdots & \frac{dr_{N_r}}{dR_{Nu}} \end{bmatrix}$$
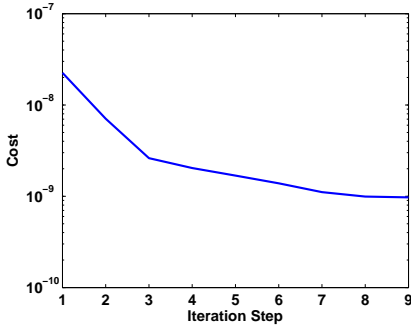(A-3)

where $\mathbf{u}$ is the unknown vector, $\mathbf{f}$ is the predicted field vector, $\mathbf{f_0}$ is the observed field vector, and the partial derivatives are obtained using finite differences by perturbing the predicted unknown parameters and calculating the corresponding residue
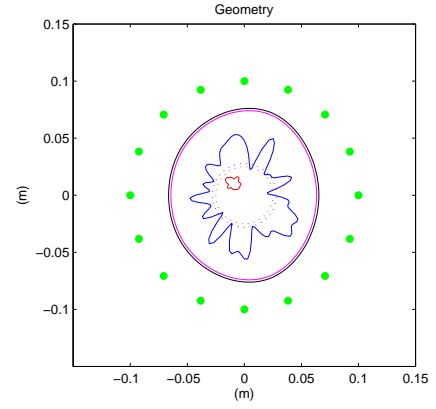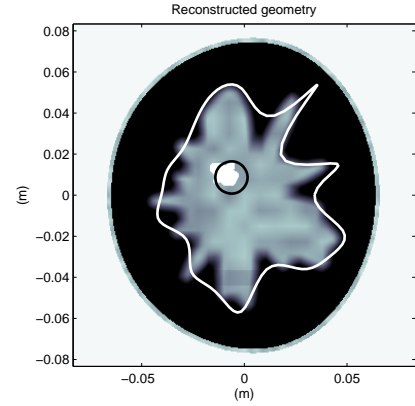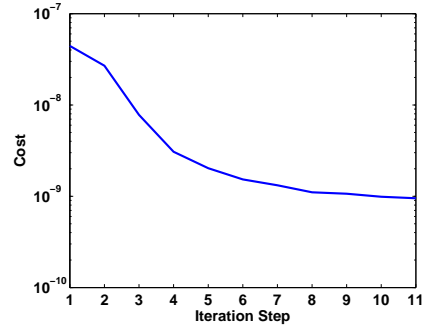
(a)

(b)

(c)

Fig. 14. Example 5: (a) Breast coronal cross-section geometry; the initial guess for dielectric properties of all layers is perturbed by 10%. (b) Reconstructed boundaries for tumor and interface (solid lines) vs. true geometry from the initial boundaries shown in Figure 14(a). (c) Cost function vs. iteration steps.

(a)

(b)

(c)

Fig. 15. Example 6: (a) Breast coronal cross-section geometry; the initial guess for dielectric properties of all layers is perturbed by 10%. (b) Reconstructed boundaries for tumor and interface (solid lines) vs. true geometry from the initial boundaries shown in Figure 14(a). (c) Cost function vs. iteration steps.

value. Hence

$$\mathbf{J}_{tum}(\mathbf{u}) = \left[\mathbf{J}_{tum}(f_1, a_1, \mathbf{u})^T, ..., \mathbf{J}_{tum}(f_{N_f}, a_{N_{rec}}, \mathbf{u})^T \right] \quad (\text{A-4})$$

$$\mathbf{J}_{int}(\mathbf{u}) = \left[\mathbf{J}_{int}(f_1, a_1, \mathbf{u})^T, ..., \mathbf{J}_{int}(f_{N_f}, a_{N_{rec}}, \mathbf{u})^T \right] \quad (\text{A-5})$$

The global Jacobian matrix is

$$\mathbf{J}(\mathbf{u}) = \left[\mathbf{J}_{tum}(\mathbf{u})^T, \mathbf{J}_{int}(\mathbf{u})^T \right] \quad (\text{A-6})$$

The global residue matrix is

$$\mathbf{r}(\mathbf{u}) = \left[\mathbf{r}(f_1, a_1, \mathbf{u})^T, ..., \mathbf{r}(f_{N_f}, a_{N_{rec}}, \mathbf{u})^T \right]^T \quad (\text{A-7})$$

Equations (A-6) and (A-7) are utilized in calculation of the gradient vector (Equation (14)) and Hessian matrix (Equation 15).

REFERENCES

[1] Breast Cancer Facts & Figures 2009-2010, American Cancer Society.

[2] S. W. Fletcher and J. G. Elmore, "Mammographic Screening for Breast Cancer," *New England Journal of Medicine*, vol. 37, pp. 1672-1680, 2003.

[3] S. Heywang-Kobrunner, R. Beck, *Contrast enhanced MRI of the breast*, 2nd edition, Berlin, Springer 1996.

[4] T. Helbich, "Contrast Enhanced magnetic resonance imaging of the breast," *European Journal of Radiology*, vol. 34, pp. 208-219, 2000.

[5] T. S. Mehta, "Current Uses of Ultrasound in the Evaluation of the Breast," *Radiologic Clinics of North America*, vol. 41, pp. 841-856, 2003.

[6] E. C. Fear, "Microwave imaging of the breast," (invited), *Technology in Cancer Research and Treatment*, vol. 4, no. 1, pp. 69-82, Feb 2005.

[7] S. Babaeizadeh and D. H. Brooks, "Electrical Impedance Tomography for Piecewise Constant Domains Using Boundary Element Shape-based Inverse Solutions, *IEEE Transactions on Medical Imaging*, vol. 26, no. 5, pp. 637-647, May 2007.

[8] P. M. Meaney, S. A. Pendergrass, M. W. Fanning, D. Li, and K. D. Pausen, "Importance of Using a Reduced Contrast Coupling Medium in 2D Microwave Breast Imaging," *J. Electromagnetic Waves and Applications*, vol. 17, pp. 333-355, 2003.

[9] D. Li, P. M. Meaney, and K. D. Paulsen, "Confocal microwave imaging for breast cancer detection," *IEEE Trans. Microwave Theory Tech.*, vol. 51, no. 4, pp. 1179-1186, Apr. 2003.

[10] P. M. Meaney, M. W. Fanning, Dun Li, S. P. Poplack, K. D. Paulsen, "A clinical prototype for active microwave imaging of the breast," *IEEE Trans. Microwave Theory and Techniques*, vol. 48, no. 11, pp. 1841-1853, Nov. 2000.

[11] E. Zastrow, S. C. Hagness, and B. D. Van Veen, "3D computational study of non-invasive patient-specific microwave hyperthermia treatment of breast cancer," *Physics in Medicine and Biology*, vol. 55, pp. 3611-3629, 2010.

[12] J. D. Shea, P. Kosmas, S. C. Hagness, and B. D. Van Veen, "Contrast-enhanced microwave imaging of breast tumors: A computational study using 3D realistic numerical phantoms," *Inverse Problems*, vol. 26, 2010.

[13] J. D. Shea, P. Kosmas, S. C. Hagness, and B. D. Van Veen, "Three-dimensional microwave imaging of realistic numerical breast phantoms via a multiple-frequency inverse scattering technique," *Medical Physics*, vol. 37, no. 8, pp. 4210-4226, August 2010.

[14] Z. Zhang and Q. Liu, "Three-dimensional Nonlinear Image Reconstruction for Microwave Biomedical Imaging," *IEEE Trans. Biomed. Eng.*, vol. 51, pp. 544-548, 2004.

[15] Z. Zhang, Q. Liu, C. Xiao, E. Ward, G. Ybarra, and W. Joines, "Microwave Breast Imaging: 3-D Forward Scattering Simulation," *IEEE Trans. Biomed. Eng.*, vol. 50, pp. 1180-1189, 2003.

[16] J. A. Bryan, Q. Liu, Z. Zhang, T. Wang, G. Ybarra, L. Nolte, and W. Joines, "Active Microwave Imaging I - 2-D Forward and Inverse Scattering Methods," *IEEE Trans. Microwave Theory Tech.*, vol. 50, pp. 123-133, 2002.

[17] A. E. Souvorov, A. E Bulyshev, S. Y. Semenov, R. H. Svenson, and G. P. Tatsis, "Two-dimensional Analysis of a Microwave Flat Antenna Array for Breast Cancer Tomography," *IEEE Trans. Microw. Theory Tech.*, vol. 48, pp. 1413-1415, 2000.

[18] A. E. Bulyshev, S. Y. Semenov, A. E. Souvorov, R. H. Svenson, A. G. Nazarov, Y. E. Sizov, and G. P. Tatsis, "Computational Modeling of Three-dimensional Microwave Tomography of Breast Cancer," *IEEE Trans. Biomed. Eng.*, vol. 48, pp. 1053-1056, 2001.

[19] S. C. Hagness, A. Taflove, and J. E. Bridges, "Two-dimensional FDTD analysis of a pulsed microwave confocal system for breast cancer detection: Fixed focus and antenna-array sensors," *IEEE. Trans. Biomed. Eng.*, vol. 45, pp. 1470-1479, Dec. 1998.

[20] S. C. Hagness, A. Taflove, and J. E. Bridges, "Three-dimensional FDTD analysis of a pulsed microwave confocal system for breast cancer detection: Design of an antenna-array element," *IEEE. Trans. Antennas Propagat.*, vol. 47, pp. 783-791, May 1999.

[21] E. C. Fear, X. Li, S. C. Hagness, and M. A. Stuchly, "Confocal microwave imaging for breast tumor detection: localization in three dimensions," *IEEE. Trans. Biomed. Eng.*, vol. 49, pp. 812-822, Aug. 2002.

[22] D. H. Staelin, A. W. Morgenthaler, and J. A. Kong, *Electromagnetic waves* Englewood Cliffs, NJ:Prentice-Hall, pp. 157-160, 1994.

[23] E. Marengo, C. M. Rappaport, and E. L. Miller, "Optimum PML ABC Conductivity Profile in FDFD," *IEEE Transactions on Magnetics*, vol. 35, pp. 1506-1509, May 1999.

[24] J. Berenger, "A perfectly matched layer for the absorption of electromagnetics waves," *J. Computat. Phys.*, vol. 114, no. 2, pp. 185-200, Oct. 1994.

[25] K. Arbter, W. E. Snyder, H. Burkhardt, G. Hirzinger, "Application of affine-invariant Fourier descriptors to recognition of 3-D objects," *IEEE Trans. Pattern Analysis and Machine Intelligence,* vol. 12, no. 7, pp. 640-647, July 1990.

[26] E. T. Whittaker, and G. Robinson, "Lagrange's Formula of Interpolation," *The Calculus of Observations: A Treatise on Numerical Mathematics*, 4th ed. New York: Dover, pp. 28-30, 1967.

[27] W. C. Karl, G. C. Verghese, and A. S. Willsky, "Reconstucting ellipsoids from projections," *Computer Vision, Graphics, and Image Processing: Graphical Models and Image Processing*, vol. 56, no. 2, pp. 124-139, March 1994.

[28] M. E. Kilmer, E. L. Miller, D. Boas, and A. Barbaro, "3d shape-based imaging for diffuse optical tomogrpahy," *Applied Optics*, 2002.

[29] C. Boor, "On calculation with B-Splines," *J. Approx. Theory*, vol. 6, pp. 50-62, 1972.

[30] C. Boor, *A Practical Guide to Splines*, New York: Springer-Verlag, 1978.

[31] L. L. Shumaker, *Spline Functions: Basic Theory*, New York, NY: Wiley, 1981.

[32] H. P. Schwan,*Electrical properties measured with alternating currents; body tissues. Handbook of Biological Data,* Philadelphia: W B Saunders Co, 1956.

[33] M. A. Stuchly and S. S. Stuchly, "Dielectric properties of biological substances - tabulated," *Journal of Microwave Power*, vol. 15, no. 1, pp. 19-26, 1980.

[34] R. Pethig, "Dielectric properties of biological materials: biophysical and medical appliications," *IEEE Trans. on Elec. Insulation*, vol. 19, pp. 453-474, Oct. 1984.

[35] W. T. Joines, Y. Zhang, C. Li, and R. L. Jirtle, "The measured electrical properties of normal and malignant human tissues from 50 to 900 MHz," *Med. Phys.*, vol. 21, pp. 547-550, 1994.

[36] F. A. Duck, *Physical Properties of Tissue: A Comprehensive Reference Book*, London: Academic Press, 1990.

[37] C. Gabriel, S. Gabriel, and E. Corthout, "The dielectric properties of biological tissues: I. Literature survey," *Phys. Med. Biol.*, vol. 41, pp. 2231-2249, 1996.

[38] R. W. Lau, S. Gabriel, and C. Gabriel, "The dielectric properties of biological tissues: II. Measurements in the frequency range 10 Hz to 20 GHz," *Phys. Med. Biol.*, vol. 41, pp. 2251-2269, 1996.

[39] S. Gabriel, R. W. Lau, and C. Gabriel, "The dielectric properties of biological tissues: III. Parametric models for the dielectric spectrum of tissues," *Phys. Med. Biol.*, vol. 41, pp. 2271-2293, 1996.

[40] A. J. Surowiec, S. S. Stuckly, J. R. Barr, and A. Swarup, "Dielectric properties of breast carcinoma and the surrounding tissues," *IEEE Trans. Biomed. Eng.*, vol. 35, pp. 257-263, 1988.

[41] S. S. Chaudhary, R. K. Mishra, A. Swarup A, and J. M. Thomas, "Dielectric properties of normal & malignant human breast tissues at radiowave & microwave frequencies," *Indian J. Biochem. Biophys.*, vol. 21, pp. 76-79, 1984.

[42] A. M. Campbell and D. V. Land, "Dielectric properties of female human breast tissue measured in vitro at 3.2 GHz," *Phys. Med. Biol.*, vol. 37, no.1, pp. 193-210, Jan. 1992.

[43] R. Luebbers, F. Hunsberger, K. Kunz, R. Standler, and M. Schneider, "A frequency-dependent finite difference time domain formulation for dispersive materials," *IEEE Trans. Electromagn. Compat.*, vol. 32, pp. 222-227, March 1990.

[44] O. Ghandi, "A frequency-dependent finite difference time domain formulation for general dipsersive media," *IEEE Trans. Microwave Theory Tech.*, vol. 41, pp. 658-665, Apr. 1993.

[45] D. M. Sullivan, "Z-transform theory and the FDTD method," *IEEE Trans. Antennas Propagat.*, vol. 55, pp. 28-34, Jan. 1996.

[46] M. Lazebnik, *et al*, "A large-scale study of the ultrawideband microwave dielectric properties of normal breast tissue obtained from reduction surgeries," *Phys. Med. Biol.*, vol. 52, pp. 2637-2656, 2007.

[47] K. Levenberg, "A method for the solution of certain problems in least squares," *Quart. Appl. Math.*, vol. 2, pp. 164-168, 1944.

[48] D. Marquardt, "An algorithm for least-squares estimation of nonlinear parameters," *SIAM J. Appl. Math.*, vol. 11, pp. 431-441, 1963.

[49] C. T. Kelley, *Iterative Methods for Optimization,* SIAM, 1999.

[50] J. Nocedal, and S. J. Wright, *Numerical Optimization*, Springer, New York, 1999.